

## Some Microstructural Aspects on Humidity-Enhanced Deterioration in the Fatigue Strength of Age-Hardened 7075 Al Alloy

**Yuzo Nakamura<sup>1,\*</sup>, Kohji Kariya<sup>2</sup>, Norio Kawagoishi<sup>2</sup>**

<sup>1</sup> Department of Mechanical Engineering, Graduate School of Science and Engineering, Kagoshima University  
Kagoshima 890-0065, Japan

<sup>2</sup> Department of Mechanical System Engineering, Daiichi Institute of Technology  
Kirishima 899-4395, Japan

\* Corresponding author: nakamura@mech.kagoshima-u.ac.jp

---

**Abstract** Age-hardened 7075 Al alloys are one of the materials which possess large strength and large toughness. Their weight and large resistance to corrosion are also attractive in practical use. We have recently shown that the fatigue behavior of extruded 7075-T6 Al alloy is strongly influenced by the humidity in atmospheric air, and the fatigue strength decreases markedly at the humidity higher than about 60%. In addition, shear-type fracture with high crack growth rate occurs at high humidity, while tensile-type fracture dominates at low humidity. The occurrence of the change in fracture mode, however, depends on the conditions used in fatigue tests. In the present study, microstructures of the 7075 T6 Al alloy subjected to fatigue tests in various conditions and humidity are examined by using electron backscattering diffraction (EBSD) and X-ray diffraction (XRD). The results of EBSD and XRD analyses indicate that the microstructures depend on the history of metalworking and heat treatment and that the fatigue properties in high humidity environment are influenced by the difference of the microstructures in addition to the effect of humidity. A crystallographic geometry model is also shown to interpret the preferential occurrence of the shear-type fracture based upon the EBSD analyses.

**Keywords** Fatigue, Humidity, Fracture mode, 7075-T6 Al alloy, Microstructure

---

### 1. Introduction

Age-hardened Al alloys are very attractive from the viewpoints of those large strength, large fracture toughness and light weight. In particular, Al-Mg-Zn(-Cu) alloys (7000 series) are commonly strengthened by the precipitation of spheric GP zone, hexagonal  $\eta'$  phase ( $\text{MgZn}_2$ ) and hexagonal  $\eta$  phase ( $\text{MgZn}_2$ ), and the degree of strengthening depends on the heat treatment conditions used for aging [1]. It is well established that 7000 series Al alloys are very susceptible to stress corrosion cracking in aggressive corrosion environment [1]. The fatigue properties of age-hardened Al alloys are very sensitive to environment, and a drastic decrease in fatigue strength occurs in the air of relative humidity (RH) higher than 85% [2]. Our previous studies [3-7] have also shown that the fatigue strength of 7075 T6 alloy decreases markedly as RH is increased to more than about 60%. Anodic dissolution of particles or stress concentration arising from large particles may become the causes of initiating cracks. However, the previous studies strongly suggest that hydrogen-enhanced local plasticity mechanism plays a major role in the deterioration of fatigue properties.

The difference in microstructure especially due to under-, peak- and over-aging has been considered to be another key issue to understand the susceptibility of age-hardened Al alloys and improve their resistance to environmental attacks. Commercial Al alloys, however, commonly experienced metalwork processes such as rolling and extrusion in order to obtain products with desired strength, shape and size. Thus, we have to consider the effect of these microstructures produced by manufacturing processes. The previous studies have shown that the extruded rods of 7075 T6 alloy exhibit unique deformation and fracture behaviors in cyclic loading. The initiation of crack and its propagation takes place at angles of about 35° inclined from the loading axis in certain atmospheres and for certain test conditions. In the rotating bend tests with the frequency of 50 Hz, this shear-type cracking is observed in high humidity more than 60% RH at high stress levels, while the decrease in

stress level or the decrease in frequency to 6 Hz alters the shear mode to the tensile mode. In the present study, microstructural analyses of the extruded 7075 T6 Al specimens subjected to fatigue tests were carried out by EBSD and XRD, in order to obtain an insight into the influence of extrusion texture on the fatigue properties in high humidity environment. Since EBSD analyses are restricted in local regions and insensitive to internal stresses, XRD analyses were also conducted to obtain the information on the macroscopic texture structure as well as the internal stresses remaining due to extrusion. The microstructural analyses were carried out on another specimen into which different microstructures were introduced by using different heat treatment. In order to deepen the understanding of the relation of fatigue properties influenced by humid environment with microstructures, some of the previous results on fatigue tests were reassessed and compared with the results of microstructural analyses.

## 2. Experimental procedure

Commercial rods of 7075 T6 Al alloy with the diameters of 18 mm were used as a starting material. The alloy has the chemical composition listed in Table 1, but the degree of extrusion was not known. Some of the as-received rods were solution treated at 733 K for 10.8 ks, and some rods were solution treated at 773 K for 118.8 ks. These solution treatments were carried out to increase grain sizes. The solution treated specimens were aged at 393 K for 86.4 ks, *i.e.*, under ordinary T6 temper condition. In order to distinguish the heat conditions, the as-received specimens and the specimens solution treated at 733 K and 773 K will be hereafter called A, B and C specimens, respectively. Table 2 shows the tensile properties and grain size of these rods. It is clear from this table that the solution treatment increased grain size considerably, and lowered the yield strength markedly compared to that of as-received ones.

The fatigue tests were conducted for A and B specimens, while C specimens were used only for the comparison of microstructure with these specimens. A specimens were subjected to rotating bend (RB) tests at 50 Hz and ultrasonic loading (US) tests at 20 kHz. On the other hand, B specimens were RB-tested at 50 Hz and 6 Hz. The shape and size of the fatigue test specimens are shown in Fig. 1. The humidity was varied from 0% RH in N<sub>2</sub> gas to 100% RH in distilled water. The details of the fatigue tests and conditions had been mentioned in the previous studies [3-7]. EBSD and XRD analyses were conducted by using disk specimens with a height of 10 mm cut from A, B and C rods (Fig. 2). The surfaces of these specimens to be used for EBSD analyses were mechanically polished to the final polishing with 20 nm silica particles, followed by low-energy Ar ion etching. XRD profiles were obtained by using Cu K $\alpha$  beam from the same transverse cross-section as was subjected to EBSD analyses. Subsequently the disc specimens were cut longitudinally at the

Table 1. Chemical composition of 7075 T6 Al.

Element	Zn	Mg	Cu	Cr	Si	Fe	Mn	Ti + Zr	Al
Mass fraction (%)	5.46	2.56	1.47	0.19	0.09	0.25	0.03	0.03	bal.
Atomic fraction (%)	2.35	2.96	0.65	0.10	0.09	0.13	0.02	0.01	bal.

Table 2. Tensile properties and grain size of 7075 T6 Al.

Specimen	Heat treatment	Yield strength (MPa)	Tensile strength (MPa)	Reduction in area (%)	Nominal grain size ( $\mu\text{m}$ )
A	as-received ordinary T6	630	691	9.5	8
B	733 K, 10.8 ks 393 K, 86.4 ks	527	673	11.3	13
C	773 K, 118.8 ks 393 K, 86.4 ks	553	685	11.6	40

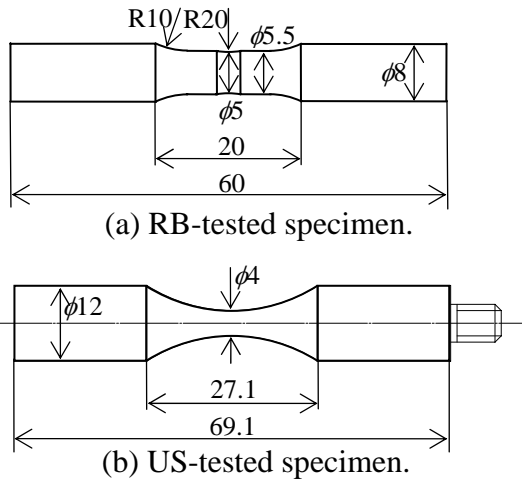


Fig. 1. Shape and size (mm) of specimens.

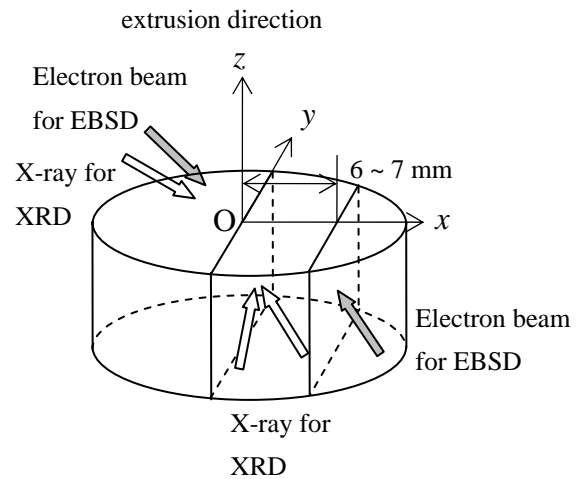


Fig. 2. Locations for EBSD and XRD analyses.

distance of 6 ~ 7 mm from the center, and the cut surfaces were polished in the same way and then subjected to EBSD and XRD analyses. In the XRD analyses of the longitudinal cross-sections, the projection of X-ray beam on the cross-section was aligned in directions along  $x$  and  $y$  axes to examine the difference in microstructure in these directions. The same procedure was applied to the microstructural analysis of longitudinal cross-sections at the center of disc.

### 3. Results

#### 3.1 Effect of humidity on fatigue strength

Fig. 3 shows a comparison of  $SN$  curves obtained for A and B specimens which are subjected to RB tests with 50 Hz in humid atmospheres ranging 0% RH ( $N_2$  gas) to 100% RH (distilled water). Symbols in the figure are experimental data of the stress amplitude ( $\sigma_a$ ) and the number of cycles to failure ( $N_f$ ), and the curves can be expressed by

$$\sigma_a = \sigma_{ao} + k\{(N_f/N_{fo})^{-m} - 1\} \quad (1)$$

where  $\sigma_{ao}$  and  $k$  are the strength coefficients,  $m$  is a numerical constant and  $N_{fo}$  is a reference number of cycles to failure and set to be  $10^7$  cycles in the present analysis. The as-received A specimens in  $N_2$  gas show the largest fatigue strength among all of the testing conditions, which exhibits larger strength by 30 ~ 60 MPa than that of B specimens fatigue-tested in  $N_2$  gas. This is consistent with the fact that the yield and tensile strengths of A specimens are larger than B specimens. Humidity does not change the fracture strength of B specimens significantly until RH is increased to 50 %, and a marked reduction of fatigue strength occurs at the humidity larger than 50 %. Previous studies showed that this transition appeared distinctly at the humidity of about 60 %. In contrast to B specimens, the humidity-induced deterioration in A specimens is prominent from the RH of 25 %, and the fatigue strength of A specimens at the humidity from 25% RH to 85% RH is lower than that of B specimens for identical RH. These results indicate that A specimens with larger yield strength is more susceptible to the environmentally assisted fatigue cracking.

Fig. 4 shows the change of the fatigue strength ( $\sigma_{ao}$ ) for  $N_f = 10^7$  as a function of RH. The fatigue strength of A specimens RB-tested at 50 Hz decreases monotonically with increasing RH. The fatigue strength of B specimens tested in the same condition, however, is insensitive to the humidity up to 50 % and shows a rapid decrease at higher humidity. Nevertheless, the fatigue strength of B specimens RB-tested at 6 Hz is kept to be constant up to 85% RH. The application of US loading with 20 kHz to A specimens results in a slight degradation from  $N_2$  gas to 25% RH, a high-stress-level plateau from 25% to 50% RH, a drastic degradation from 50% to 75% RH, and

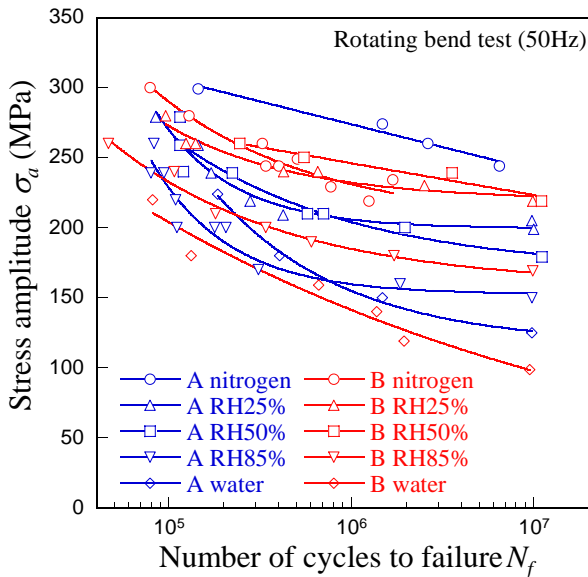


Fig. 3. SN curves of A and B specimens.

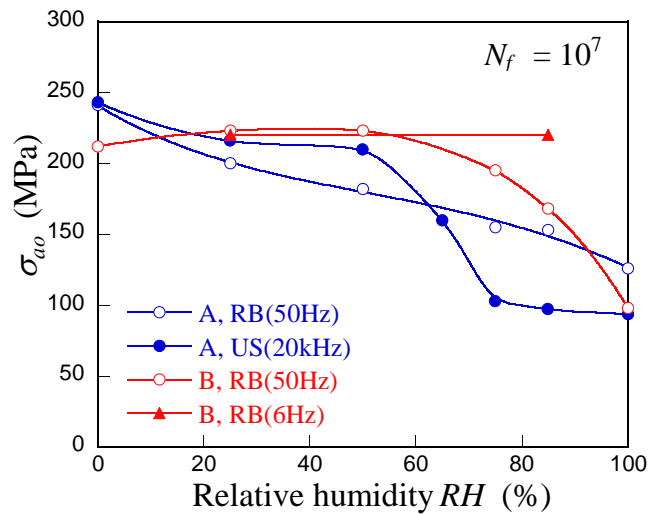


Fig. 4. Dependence of fatigue strength on RH.

then a low-stress-level plateau above 75% RH. It is obvious that these different fatigue behaviors cannot be explained only by the effect of humidity.

### 3.2 Crack initiation and growth

SEM observations conducted in previous studies [3-7] showed different morphologies of fatigue cracks in extruded 7075 T6 Al alloy, which are depicted schematically in Fig. 5 (a)~(d). These morphologies are macroscopically classified into (a) tensile-mode-initiation followed by tensile-mode-propagation (TT-type), (b) tensile-mode-initiation and shear-mode-propagation (TS-type), (c) shear-mode-initiation and shear-mode-propagation (SS-type), and (d) multiple-shear-mode-initiation followed by coalescence of cracks leading to apparent tensile fracture (MST-type). Typical examples of fracture surfaces are also shown in Fig. 5. In A specimens RB-tested at 50 Hz, crack initiation takes place in tensile manner and their macroscopic fracture mode becomes TT-type in all of the humid conditions and TS-type in N<sub>2</sub> gas. On the other hand, the application of US loading to A specimens changes the crack initiation from tensile mode to shear mode, except at low humidity. Hence US-tested A specimens show TS-type fracture at low humidity and SS-type or MST-type fracture for other conditions. This tendency appears in B specimens RB-tested at 50 Hz, too. The common feature to US-tested A specimens and RB-tested B specimen is that MST-type fracture is induced at 85% RH and in water at low stress level. This fact suggests that many cracks are initiated at the surface exposed to such high humidity for longer time. Both of the initiation and propagation of S-type cracks take place at an angle of about 35° inclined from the loading axis in both of the RB and US tests. In particular, the morphologies of initial cracks are important, since they may be indicative of the slip prior to the initiation as well as the slip associated with the initiation.

Fig. 6 shows typical examples of T-type and S-Type short cracks observed on the surfaces of B specimens RB-tested at 25% RH and 85 % RH, respectively. The T-type crack exhibits some irregularities in propagation path, some of which are inclined by ±35° from the loading axis, but it develops in a direction perpendicular to the loading axis. On the other hand, the S-type crack develops in a shape of "V" of which edges are symmetrically inclined by ±35° from the loading axis. The symmetry of crack initiation with a definite geometry, which can be microscopically observed in the zigzag path of T-type crack, indicates that slip leading to the crack initiation may take place

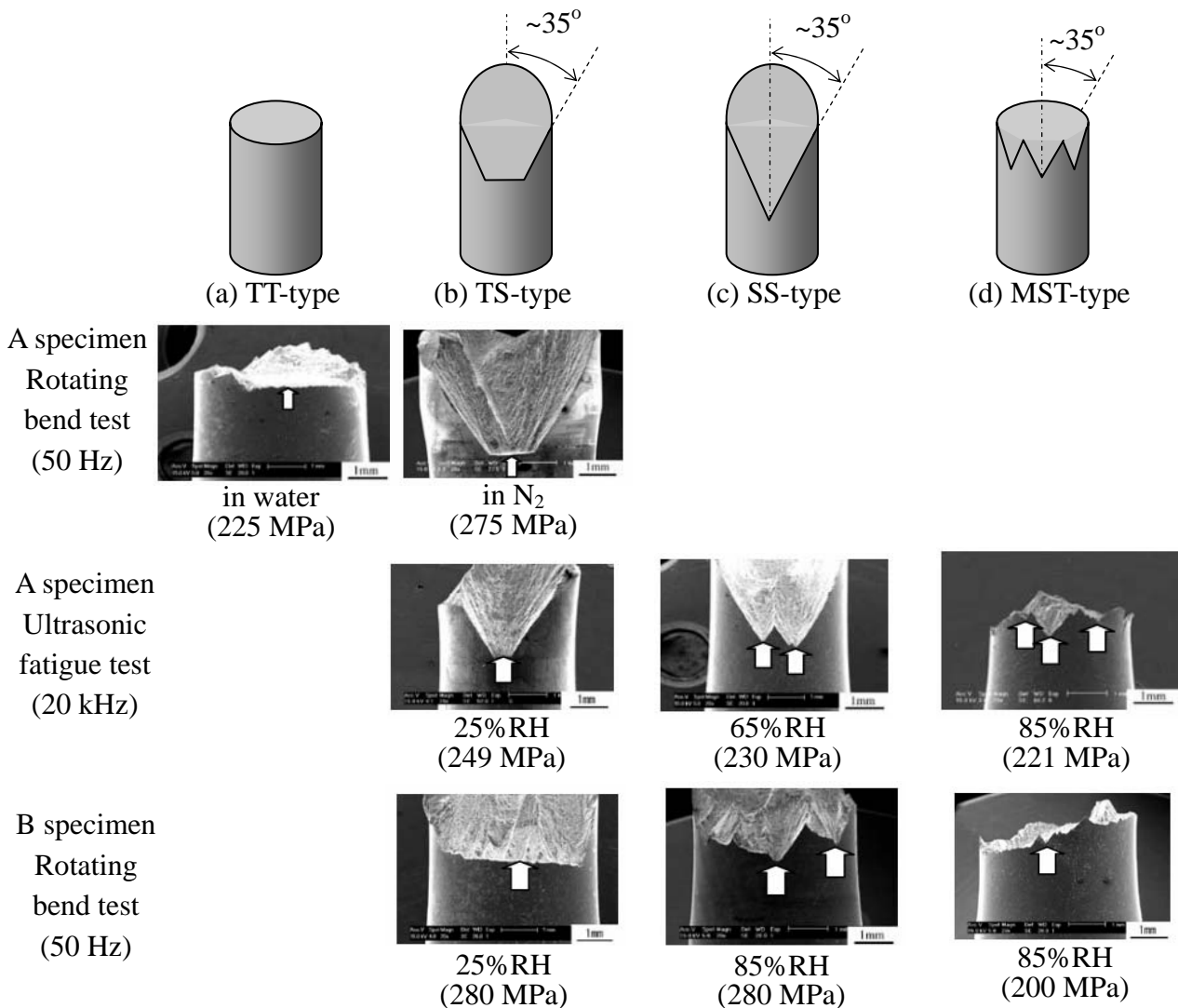


Fig. 5. Macroscopic features of fatigue fracture.

preferentially in this direction. One can see that the crack propagation in macroscopic scale shows the same tendency in certain circumstances. Thus, the evolution of plastic zone in front of crack tip may also have orientation-dependence intrinsic to the microstructure.

Fig. 7 shows typical relations of crack length ( $l$ ) and number of cycles ( $N$ ) in B specimens RB-tested at 50 Hz. The values of crack length were measured in transverse direction. Thus the length of a pure S-type crack developing with an angle of  $35^\circ$ , for example, becomes  $l/\sin 35^\circ = 1.74l$ . As shown in Fig. 5, there are some mixtures of T- and S-type crack propagations so that the real length of crack along its path is always larger than the measured value of  $l$  in such mixtures. Reminding this effect, one can see from Fig. 6 that the growth of S-type cracks formed at 85% RH occurs much faster than that of T-type cracks at 25% RH. It is also recognized that the initiation of S-type cracks at such high humidity is induced at very small cycles compared with the initiation of T-type cracks at low humidity. On the other hand, A specimens tested in the same test condition show T-type crack initiation irrespectively of environment, while its sensitivity to humid environment appears from low humidity. US tests with 20 kHz enables A specimens to exhibit the S-type cracking so that the crack growth as a function of  $N$  becomes much larger than RB-tested A specimens. This result suggests that the formation and propagation of cracks may be rate-controlled. This was also demonstrated in B specimen; the reduction of frequency from 50 Hz to 6 Hz in RB tests transformed the fracture mode from S-type to T-type [7].

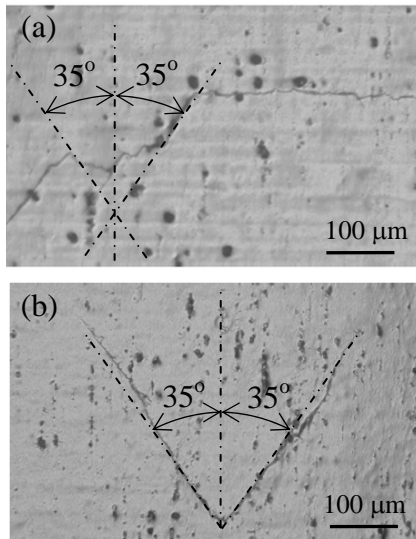


Fig. 6. Crack initiations in (a) T-type and (b) S-type modes.

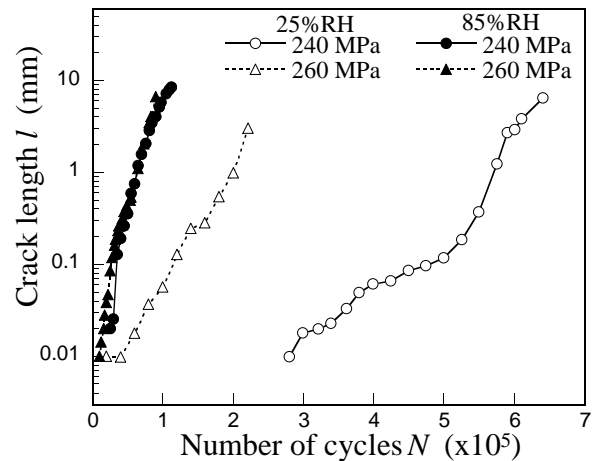


Fig.7. Relation of crack growth with the number of cycles in B specimens.

### 3.3 Microstructure

Fig. 8(a) shows the SEM image of the transverse cross-section at the center of B specimen, which is inclined by  $70^\circ$  for EBSD analyses. Fig. 8 (b), (c) and (d) are the maps (IPF maps) of crystallographic orientations of grains in  $z$ ,  $x$  and  $y$  directions, respectively, which are obtained from the square region depicted in Fig. 8(a). Grains are distinguishable by those relief and contrast in SEM image. The grain size estimated by using the SE image is  $12\ \mu\text{m}$ , which is nearly the same as the grain size evaluated by using large misorientation angle. The IPF image along  $z$  axis shows that the transverse surface are dominated by large grains close to  $\langle 111 \rangle$  direction (hereafter called  $\langle 111 \rangle$  grains) and the remaining large grains have orientations close to  $\langle 001 \rangle$  (hereafter called  $\langle 001 \rangle$  grains). The areal fraction of  $\langle 111 \rangle$  grains is estimated to be about 80 %. However, the IPF images along  $x$  and  $y$  axes clearly indicate that these large grains involve subgrains, and the average grain size including the subgrains is estimated to be  $3.9\ \mu\text{m}$  by using a misorientation angle of  $0.5^\circ$  for grain boundary detection. The IPF (Fig. 7(e)) along  $z$  axis also shows the largest fraction of  $\langle 111 \rangle$  grains and the second one of  $\langle 001 \rangle$  grains. The crystallographic orientations are uniformly distributed along  $\langle 101 \rangle$ - $\langle 112 \rangle$  circle in  $x$  and  $y$  directions, as is shown by Figs. 7(f) and 7(g).

Figs. 9 and 10 are the IPF images of A and C specimens, respectively. It is obvious that the grains in C specimens have round corners compared to A specimens, which indicates the grain growth takes place in C specimen by the solution treatment. The grain growth appearing as round grains can be seen in B specimen by comparing Fig. 8(b) with Fig. 9(a). The grain sizes listed in Table 4 show that the as-received A specimen has the smallest grain sizes in both large misorientation and small misorientation including subgrains. In addition the fraction of  $\langle 111 \rangle$  grains in A specimen is 61 %, while the fraction in the other specimens are nearly 80%. This result indicates that the solution treatments done for B and C specimens induce the preferential growth of  $\langle 111 \rangle$  grains.

Fig. 11(a), (b) and (c) are the pairs of IPF image and IP figure taken from the longitudinal cross-section at the center of B specimen along  $z$ ,  $x$  and  $y$  axes, respectively. The longitudinal cross-section is mainly covered with  $\langle 111 \rangle$  grains which involve the elongated islands of  $\langle 001 \rangle$  grains (Fig. 11(a)). The extrusion ratio is estimated to be more than 800 % from the shape of island  $\langle 001 \rangle$  grains. In contrast to the transverse cross-section, subgrains involved in large  $\langle 111 \rangle$  grains do not have large misorientation between neighboring ones. It is also noted that some of the  $\langle 001 \rangle$  grains observed in  $z$  axis analysis disappear in  $x$  and  $y$  axes, which indicate that these disappeared grains have continuous relation with surrounding  $\langle 111 \rangle$  grains. Thus the texture structure is

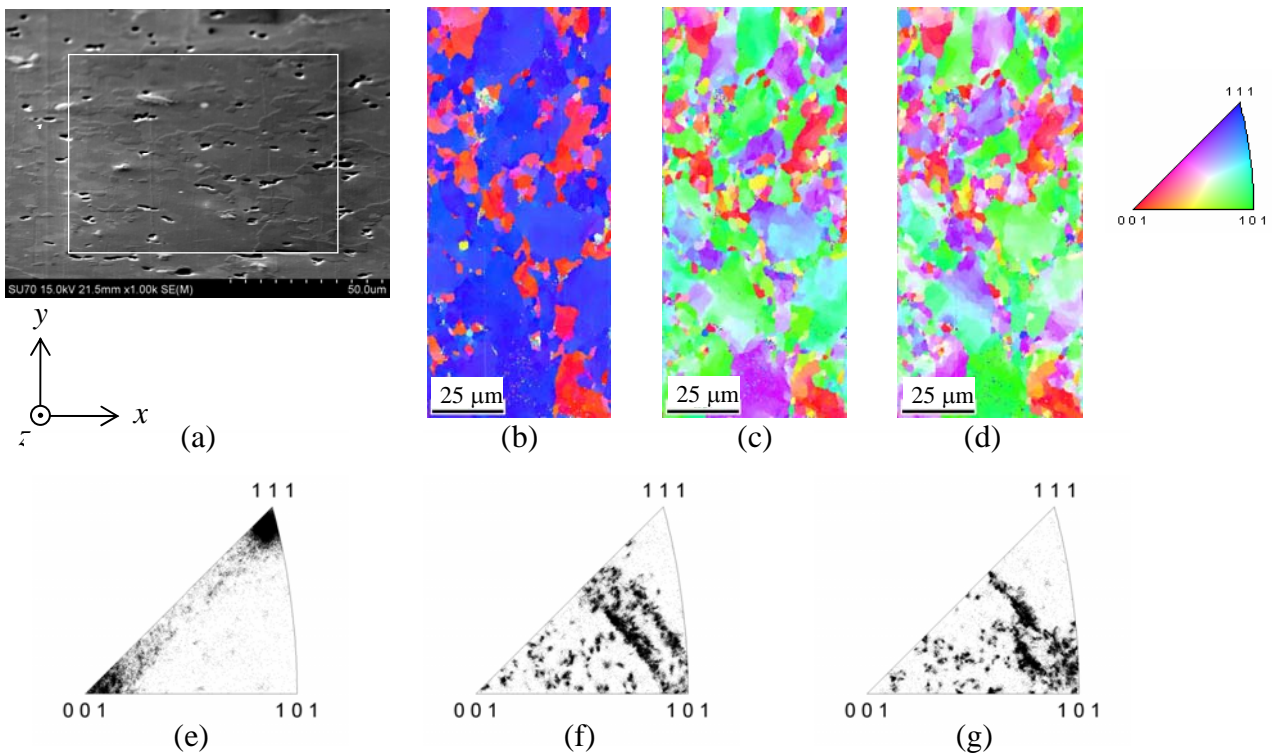
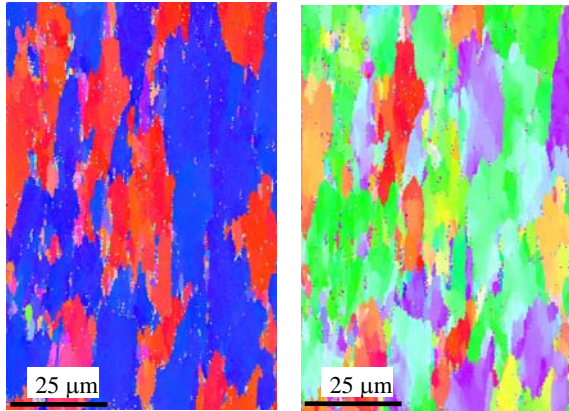
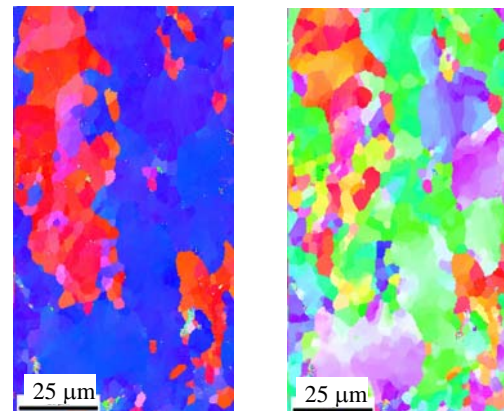


Fig. 8. Results of EBSD analyses obtained for the transverse cross-section at center of B specimen. (a) SE image, (b) IPF map along z axis, (c) IPF map along x axis, (d) IPF map along y axis, (e) IP figure along z axis, (e) IP figure along x axis, and (f) IP figure along y axis.



(a) z axis (b) x axis  
Fig. 9. IPF maps of transverse cross-section at center of A specimen.



(a) z axis (b) x axis  
Fig. 10. IPF maps of transverse cross-section at center of C specimen.

consisted of fibrous grains of  $3.9 \mu\text{m}$  diameter elongated in the extrusion direction, but is regarded as having the single-crystal-like nature within several  $10 \mu\text{m}$  in the transverse directions. These trends are common in all specimens investigated. However A specimen exhibits a larger fraction of  $\langle 001 \rangle$  grains, as is shown in Fig. 9 (a).

### 3.4 XRD profiles

Fig. 12 shows the XRD peaks taken from the transverse cross-section in B specimen. The height of (111) reflection peak was considerably large in all of the specimens due to the texture of  $\langle 111 \rangle$

Table 4. Estimated grain sizes and fraction of <111> grains.

Specimen	Grain size with large misorientation ( $\mu\text{m}$ )	Grain size involving subgrains ( $\mu\text{m}$ )	Fraction of <111> grains (%)
A	10	1.8	61
B	12	3.9	80
C	50	5.5	85

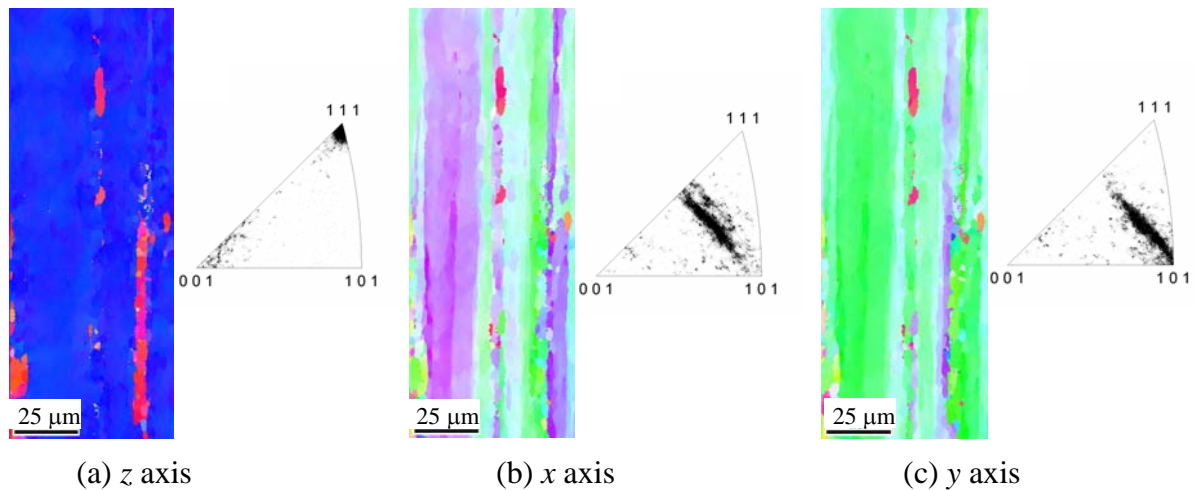


Fig. 11. IPF images and IP figures of longitudinal cross-section at center of B specimen.

grains, as is typically demonstrated by Fig. 12. This result is consistent with the results of EBSD analyses mentioned above. However, A specimen has the broadest peaks, while C specimen has the most narrow peaks, as shown in Fig. 13. Since the grain sizes of the present specimens are too large to contribute to the broadening of XRD peaks, the internal stress is attributed to the broadening in A and B specimens [6]. The internal stress due to precipitates is considered to be nearly the same in all specimens, because the same aging condition is applied. Therefore the broadening of XRD peaks is considered to be brought by the difference in the dislocation density; A specimen has the largest dislocation density, the density in B specimen is the second largest and the density in C specimen is comparable to that of the annealed one which shows distinct peaks of  $K_{\alpha 1}$  and  $K_{\alpha 2}$  X-rays.

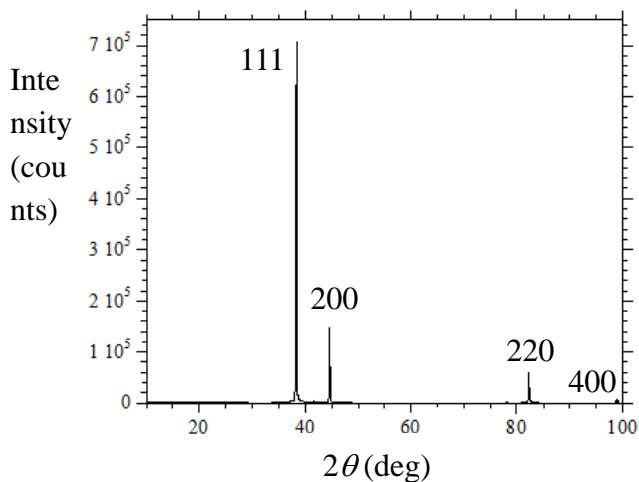


Fig. 12. X ray peaks in B specimen.

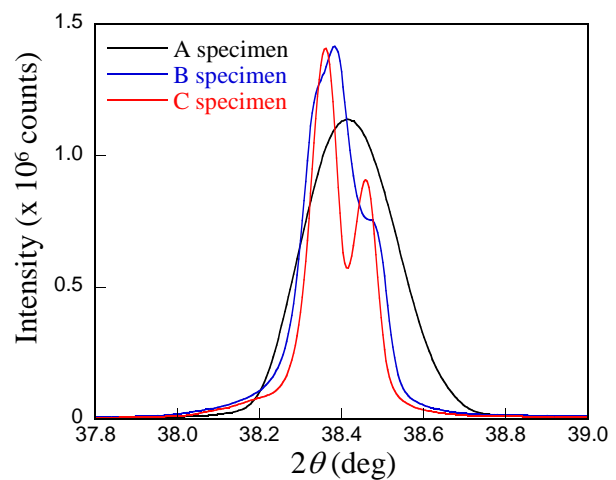


Fig. 13. Peaks of (111) reflection.

## 4. Discussion

Birnbaum and Solfronis [8] calculated the interaction of H interstitials with dislocations and indicated that the motion of dislocations trapping H interstitials becomes easier and planar. Ferreira *et al.* [9] showed that the cross slip of screw dislocations in pure Al becomes difficult in hydrogen atmosphere. Further, Bond *et al.* [10] showed that the velocity of dislocations is enhanced and therefore the resistance to cracking is reduced in 7050 and 7075 alloys exposed to hydrogen atmosphere. These theoretical and experimental results strongly support that hydrogen-enhanced local plasticity (HELP) accompanying the reduction of flow stress and the planar slip is induced in Al and its alloys, when they are exposed to environments which enable H atoms to enter the materials. It is also considered that H atoms formed by the reaction of H<sub>2</sub>O with freshly created surfaces close to crack tips enter the material during the fatigue cracking of 7075 T6 alloy in high humidity. The HELP mechanism works at the crack tips and lowers the flow stress in the plastic zone in front of the crack tips. This deterioration mechanism explains the present results well. However, the difference in the sensitivity to humidity as well as the fracture mode between A and B specimens, which is shown by Figs. 3-7, has not been made clear [13].

As mentioned in sections 3.3 and 3.4, as-received A specimens have finer grains containing dislocations with a high density. In contrast, B specimens solution-treated at 733 K for 10.8 ks exhibit the preferential growth of  $\langle 111 \rangle$  grains and their dislocation density is lowered. Such grain growth as well as the reduction in dislocation density is manifested in C specimens. These results suggest that the grain size, the structure of texture and the dislocation density influence the HELP mechanism in environmentally assisted fatigue cracking. In A specimens, both of the  $\langle 111 \rangle$  and  $\langle 100 \rangle$  grains are relatively hard as is shown by the yield strength in Table 2. In addition, the fraction of  $\langle 100 \rangle$  grains in A specimens is larger compared with that of B specimens. It is hence considered that the propagation of slip between neighboring grains is more difficult in A specimens. On the other hand, the grains in B specimens are softer and mostly governed by  $\langle 111 \rangle$  grains, and the misorientations between the subgrains are very small (Fig. 11). Therefore it is considered that the texture structure of B specimens enables selected slips to propagate smoothly from grain to grain. This consideration explains well why the shear mode fracture takes place more preferentially in B specimens than in A specimens under the same RB test condition using 50 Hz (Fig. 5).

Kariya [11] found by using etch pit technique that the humidity-induced shear mode cracks propagate in  $\langle 110 \rangle$  direction and the cracks lie on  $\{001\}$  plane in B specimens RB-tested at 50 Hz. This result seems to be consistent with the morphology of observed S-type cracks, since the angle between  $\langle 111 \rangle$  and  $\langle 001 \rangle$  is  $35.3^\circ$ . On the other hand, the present EBSD analyses yield such angle of S-type cracks in other geometries as shown in Fig. 14. In a  $\langle 100 \rangle$  grain, the intersections of two slip planes with the specimen surface make the angle of  $\pm 35.3^\circ$ , when  $\langle 110 \rangle$  direction of the grain is normal to the surface (Fig. 14(a)). The "V"-shaped crack can be formed only in this geometry. In a  $\langle 111 \rangle$  grain, a slip direction makes an angle of  $35.3^\circ$  with the specimen surface, when this slip direction is parallel to the surface (Fig. 14(b)). It is suspected from these geometries that the cracks of "V" shape are initiated in such  $\langle 100 \rangle$  grains emerging at the specimen surface. It should be also noted that the "V"-shaped cracks in  $\langle 100 \rangle$  grains can induce the slip in neighboring  $\langle 111 \rangle$  grains with the same angle, when  $\langle 011 \rangle$  directions of both grains are aligned like Fig. 14(a) and (b). Further the slip in  $\langle 100 \rangle$  grains can be continuously connected with the slips in  $\langle 111 \rangle$  grains, when the slips on two slip planes involving the selected direction operate simultaneously in  $\langle 111 \rangle$  grains. This situation leads to the macroscopic  $\{001\}$  slip plane in  $\langle 111 \rangle$  grains which is microscopically composed of two slip planes (Fig. 14(c)). As a result,  $\{111\}$  and  $\{001\}$  planes become preferential planes for crack propagation in  $\langle 100 \rangle$  and  $\langle 111 \rangle$  grains, respectively. It is also considered that edge dislocations glide on these planes so that the interaction of H atoms with the edge dislocations induces the acceleration of inclined crack propagation. It is suspected that the continuous slip propagation between  $\langle 100 \rangle$  and  $\langle 111 \rangle$  grains in A specimens is more difficult than in B specimens

for the reasons mentioned above. In the present study, we have not yet obtained the full understanding on the mechanisms by which the fatigue properties are influenced by the test conditions such as RB, US and frequencies. It is believed that such effects involve some rate-controlled processes like the diffusion and trapping of H atoms in different microstructures.

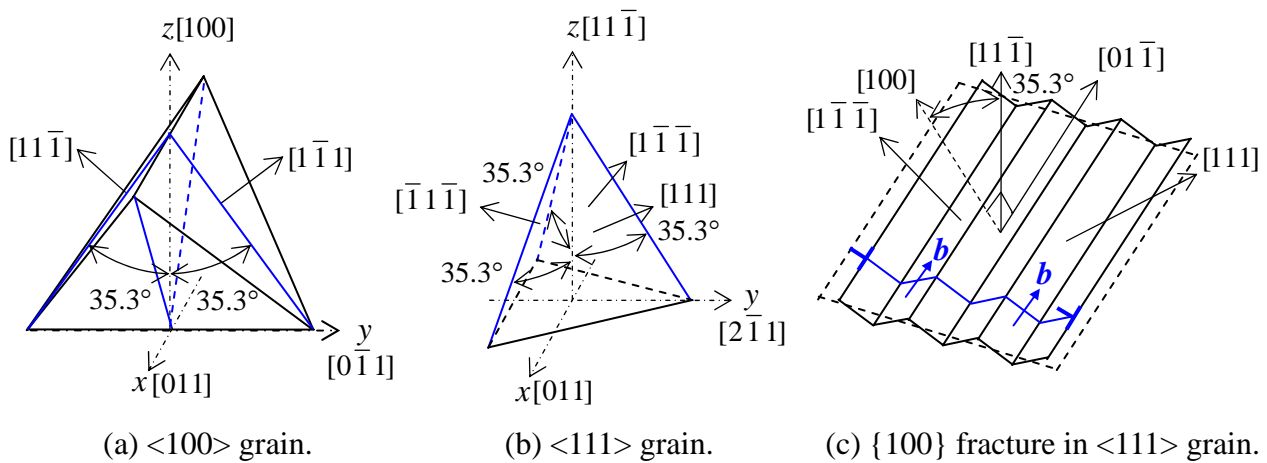


Fig. 14 Crystallographic geometries. Thompson tetrahedron is used in (a) and (b).

## 5. Summary

The present study shows that extruded 7075 T6 Al alloy exhibits the deterioration of fatigue strength in high humidity environment. However the fracture mode strongly depends not only on the history of the metalworking and heat treatment, but also on the test conditions. The results of EBSD and XRD analyses indicate that these differences may arise from the grain size, texture structure and dislocation density. In particular, the shear mode cracking with the angle of  $35^\circ$  from loading axis can be correlated with the crystallographic geometry of slips which are selected in the texture strongly aligned in  $\langle 111 \rangle$  direction. In order to interpret the whole phenomena including the test conditions, more analyses taking into the characteristics of microstructures will be needed.

## References

- [1] I.J. Polmear, Light Alloys, Second Edition, Edwald Arnold, London, 1989.
- [2] N.E. Frost, K.J. Marsh, L.P. Pook, Metal Fatigue, Dover, New York, 1999.
- [3] N. Kawagoshi, T. Fukudome, Y. Nakamura, Y. Ozono, M. Goto, J JSME A, 76 (2010) 938-946.
- [4] K. Kariya, N. Kawagoishi, T. Fukudome, Y. Nakamura, E. Kondo, J-JSMS, 60 (2011) 339-344.
- [5] N. Kawagoishi, K. Kariya, Q. Chen, M. Goto, Y. Nakamura, J-JSMS, 60 (2011) 890-897.
- [6] K. Kariya, N. Kawagoishi, S. Furumoto, Y. Nakamura, E. Kondo, J-JSMS, 60 (2011) 1015-1022.
- [7] K. Kariya, H. Maeda, N. Kawagoishi, Q. Chen, Y. Nakamura, K. Morino, J-JSMS, 61 (2012) 712-718.
- [8] A. Guinier, X ray Diffraction in Crystals, Imperfect Crystals, and Amorphous Bodies, Dover, New York, 1994.
- [9] C.D. Beacham, Met Trans, 3 (1972) 437-451.
- [10] H.K. Birnbaum, P. Sofronis, Mater Sci Eng, A176 (1994) 191-202.
- [11] P.J. Ferreira, I.M. Robertson, H.K. Birnbaum, Acta Mater, 47 (1999) 2991-2998.
- [12] G.M. Bond, I. M. Robertson and H. K. Birnbaum, Acta Metall, 35 (1987) 2289-2296.
- [13] K. Kariya, Doctoral Thesis, Kagoshima University, Japan (2012).